doi:10.1093/brain/awx353 BRAIN 2018: 141; 568–581 | 568

BRAIN
A JOURNAL OF NEUROLOGY

Networks of tau distribution in Alzheimer's disease

Merle C. Hoenig,[1] Gérard N. Bischof,[1,2] Joseph Seemiller,[3] Jochen Hammes,[1] Juraj Kukolja,[2,4] Özgür A. Onur,[2,4] Frank Jessen,[5,6] Klaus Fliessbach,[6,7] Bernd Neumaier,[8,9] Gereon R. Fink,[2,4] Thilo van Eimeren[1,2,4,6] and Alexander Drzezga[1,6]

See Whitwell (doi:10.1093/brain/awy001) for a scientific commentary on this article.

A stereotypical anatomical propagation of tau pathology has been described in Alzheimer's disease. According to recent concepts (network degeneration hypothesis), this propagation is thought to be indicative of misfolded tau proteins possibly spreading along functional networks. If true, tau pathology accumulation should correlate in functionally connected brain regions. Therefore, we examined whether independent components could be identified in the distribution pattern of *in vivo* tau pathology and whether these components correspond with specific functional connectivity networks. Twenty-two ^{18}F-AV-1451 PET scans of patients with amnestic Alzheimer's disease (mean age = 66.00 ± 7.22 years, 14 males/eight females) were spatially normalized, intensity standardized to the cerebellum, and z-transformed using the mean and deviation image of a healthy control sample to assess Alzheimer's disease-related tau pathology. First, to detect distinct tau pathology networks, the deviation maps were subjected to an independent component analysis. Second, to investigate if regions of high tau burden are associated with functional connectivity networks, we extracted the region with the maximum z-value in each of the generated tau pathology networks and used them as seeds in a subsequent resting-state functional MRI analysis, conducted in a group of healthy adults (n = 26) who were part of the 1000 Functional Connectomes Project. Third, to examine if tau pathology co-localizes with functional connectivity networks, we quantified the spatial overlap between the seed-based networks and the corresponding tau pathology network by calculating the Dice similarity coefficient. Additionally, we assessed if the tau-dependent seed-based networks correspond with known functional resting-state networks. Finally, we examined the relevance of the identified components in regard to the neuropathological Braak stages. We identified 10 independently coherent tau pathology networks with the majority showing a symmetrical bi-hemispheric expansion and coinciding with highly functionally connected brain regions such as the precuneus and cingulate cortex. A fair-to-moderate overlap was observed between the tau pathology networks and corresponding seed-based networks (Dice range: 0.13–0.57), which in turn resembled known resting-state networks, particularly the default mode network (Dice range: 0.42–0.56). Moreover, greater tau burden in the tau pathology networks was associated with more advanced Braak stages. Using the data-driven approach of an independent component analysis, we observed a set of independently coherent tau pathology networks in Alzheimer's disease, which were associated with disease progression and coincided with functional networks previously reported to be impaired in Alzheimer's disease. Together, our results provide novel information regarding the impact of tau pathology networks on the mechanistic pathway of Alzheimer's disease.

1 Multimodal Neuroimaging Group, Department of Nuclear Medicine, University Hospital Cologne, Cologne, Germany
2 Cognitive Neuroscience, Institute of Neuroscience and Medicine (INM-3), Research Center Juelich, Juelich, Germany
3 Geisinger Commonwealth School of Medicine, Scranton PA, 18509, USA
4 Department of Neurology, University Hospital Cologne, Cologne, Germany
5 Department of Psychiatry, University Hospital Cologne, Cologne, Germany
6 German Center for Neurodegenerative Diseases (DZNE), Bonn/Cologne, Germany
7 Department of Neurodegenerative Diseases and Geriatric Psychiatry, University Hospital Bonn, Bonn, Germany
8 Nuclear Chemistry, Institute of Neuroscience and Medicine (INM-5), Research Center Juelich, Juelich, Germany
9 Institute of Radiochemistry and Experimental Molecular Imaging, University Hospital Cologne, Cologne, Germany

Received May 11, 2017. Revised October 19, 2017. Accepted November 8, 2017. Advance Access publication January 5, 2018

Correspondence to: Merle Hönig, MSc
Department of Nuclear Medicine, University Hospital Cologne, Building 60, Kerpener Str. 62, 50937 Cologne, Germany
E-mail: merle.hoenig@uk-koeln.de

Keywords: tau pathology networks; PET; independent component analysis; resting-state networks

Abbreviations: DMN = default mode network; DSC = Dice similarity coefficient; ICA = independent component analysis; SUVR = standard uptake value ratio; TPN = tau pathology network

Introduction

Alzheimer's disease is characterized by two neuropathological hallmarks, i.e. the accumulation of extracellular amyloid-β plaques and the intracellular aggregation of misfolded tau proteins in form of neurofibrillary tangles. Amyloid-β pathology initially spreads across neo- and allocortical brain regions and only propagates downstream to the brainstem in late stages of the disease (Thal *et al.*, 2002), whereas tau pathology first occurs in the locus coeruleus and the entorhinal cortex from where it expands upstream to limbic and isocortical regions (Braak and Braak, 1991, 1995). Several hypotheses have been suggested to explain the spreading and distribution of these pathologies across the brain. One prominent proposal is the network degeneration hypothesis, which postulates that neurodegenerative disease pathologies expand along functional networks, consequently leading to failure of these networks (Palop *et al.*, 2006; Seeley *et al.*, 2009). Network dysfunction then in turn likely provokes clinical symptomatology. In the past decade, multimodal imaging studies have provided compelling evidence in support of the network degeneration hypothesis: a spatial overlap between the deposition of amyloid-β plaques and neuronal networks, in particular the default mode network (DMN), has been reported (Buckner *et al.*, 2005, 2009; Grothe and Teipel, 2016; Jones *et al.*, 2016). Similar results were obtained when investigating the convergence between Alzheimer's disease-related grey matter volume reduction and large-scale networks (Seeley *et al.*, 2009). Furthermore, it was suggested that elevated amyloid-β deposition in regions of the DMN in asymptomatic cognitively normal individuals could serve as an indicator of incipient Alzheimer's disease (Sperling *et al.*, 2009). So far, it remains unknown whether tau pathology similarly expands along functional networks as the visualization of tau pathology *in vivo* has only recently become available. However, the stereotypical anatomical distribution pattern of tau pathology is indicative of misfolded tau proteins spreading throughout interconnected regions (Clavaguera *et al.*, 2009). This assumption is supported by recent findings from studies in rodent models of early Alzheimer's disease proposing that neurofibrillary tangles may exhibit prion-like properties (Clavaguera *et al.*, 2009; de Calignon *et al.*, 2012; Liu *et al.*, 2012). These properties may foster the spreading of tau pathology through axons and across synapses to other neurons, potentially consecutively affecting connected brain regions and eventually leading to severe neurodegeneration that causes cognitive impairment.

With the development of PET ligands for the visualization of tau depositions, disease-specific distribution patterns of tau pathology can now be detected and studied in humans *in vivo*. The radioactive tracer ^{18}F-AV-1451 appears especially useful for the visualization of separate patterns of tau pathology distribution within the Alzheimer's disease spectrum (Ossenkoppele *et al.*, 2016; Dronse *et al.*, 2017), and across different tauopathies (Passamonti *et al.*, 2017). To assess distinct pathways of Alzheimer's disease-related tau pathology based on ^{18}F-AV-1451 PET imaging data, the multivariate approach of an independent component analysis (ICA) may represent a particularly well-suited tool. ICA is a blind source separation technique used to establish common features within a given dataset by decomposing the data into independent patterns (McKeown *et al.*, 2003). ICA is based on a whole-brain data-driven approach that is not limited to a set of predefined regions of interest (Fan *et al.*, 2008). Even though ICA has often been used to study properties of brain networks based on functional MRI data (Calhoun and Adali, 2012), several studies also confirmed the utility of ICA for the analysis of PET data (Illán *et al.*, 2011; Di *et al.*, 2012; Toussaint *et al.*, 2012; Shaffer *et al.*, 2013; Yakushev *et al.*, 2013; Savio *et al.*, 2017). For example, ICA identified distinct metabolic networks in ^{18}F-fluorodeoxyglucose-PET scans, which resembled known resting-state functional connectivity networks (Di *et al.*, 2012; Yakushev *et al.*, 2013; Savio *et al.*, 2017).

Using ICA within the realm of structural or functional brain imaging analyses, regions within an independent component can be inferred to be spatially correlated either through structural or functional connections (Cohen *et al.*, 2008; Di *et al.*, 2012). However, the detection of independent components in PET imaging data does not necessarily allow drawing of conclusions about the functional or structural connections of the associated brain regions within given independent components. Consequently, systematic comparison of such components with information on existing functional or structural networks is required.

Here, to gain insights into the mechanistic pathways of tau pathology and to identify independent tau pathology networks (TPNs), we used an ICA approach on ^{18}F-AV-1451 tau-PET imaging data of 22 patients with mild-to-moderate amnestic Alzheimer's disease. Subsequently, we systematically assessed the relationships between the

identified TPNs and the functional network architecture of the brain. For this purpose, we first extracted the region of maximum tau deposition from each of the generated TPNs. Next, we used these regions as seeds for a seed-based resting-state functional MRI analysis in a group of healthy control subjects (derived from the 1000 Functional Connectomes Project). The seed-based networks were established to identify regions of strongest connections to the seed of tau pathology of a given TPN. We assessed the spatial conformity of these (tau-dependent) functional connectivity networks with the detected TPNs as well as with established functional resting-state networks (Shirer *et al.*, 2012). Finally, we assessed whether higher tau burden in the identified TPNs was associated with a more advanced Braak stage as well as global cognitive dysfunction as assessed by the Mini-Mental State Examination (MMSE). We hypothesized that the ICA would yield TPNs that coincide with functionally connected networks resembling known resting-state networks, such as the DMN. Moreover, we assumed that increased tau burden within distinct TPNs would be associated with a more advanced Braak stage and negatively correlate with global cognitive function.

Materials and methods

Participants

We included 22 patients with typical amnestic Alzheimer's disease (Table 1) who were diagnosed with probable Alzheimer's disease dementia according to the recommended NIA-AA guidelines (McKhann *et al.*, 2011) and based on the results of diagnostic PET imaging and CSF measurements. Of the 22 patients, 16 patients were amyloid-positive (based on their amyloid PET scan). In addition, three patients were amyloid-positive based on the assessment of their CSF. In the remaining three patients, diagnosis of Alzheimer's disease was established without assessment of amyloid status, based on the NIA-AA guidelines. All patients underwent an ^{18}F-AV-1451 PET scan as part of their clinical evaluation in the Department of Nuclear Medicine at the University Hospital Cologne, Germany, and gave informed consent for the scientific evaluation and publication of their data. Key inclusion criteria for the patient sample were: (i) diagnosis of probable typical Alzheimer's disease according to the NIA-AA criteria; (ii) age range: >55 and $\leqslant 80$ years; and (iii) evaluable ^{18}F-AV-1451 scan. The study was performed according to the Declaration of Helsinki and was in compliance with the requirements of the ethics board of the Faculty of Medicine at the University of Cologne and of the responsible local regulatory authorities.

Table 1 Demographic characteristics

Characteristic	Mean ± SD	Min	Max
Age	66.00 ± 7.22	55	75
Education	13.80 ± 3.11	8	18
MMSE	24.45 ± 4.38	15	30
Sex	M = 14; F = 8		
Race	Caucasian		

The range and average age in years, years of education, level of cognitive dysfunction as assessed by the Mini-Mental State Examination (MMSE), sex distribution, and race are listed in this table. F = female; M = male; SD = standard deviation.

PET data

The PET scans were collected from a PET-CT Siemens Biograph mCT Flow 128 Edge (Siemens). A low dose transmission scan was performed with CT for attenuation correction prior to the beginning of the PET scanning. PET scans were acquired in list mode (15 min) 90 min after an intravenous injection of a mean dose of 230 MBq of ^{18}F-AV-1451. The scans were iteratively reconstructed using a 3D OSEM algorithm of four iterations and 12 subsets, and were smoothed with a Gaussian filter of 5 mm full-width at half-maximum on a 128 × 128 matrix.

Resting-state functional MRI data

To identify functional networks in a group of healthy adults, we used the publicly available resting-state functional MRI dataset by Berlin-Margulies (Rohr *et al.*, 2013), which is part of the 1000 Functional Connectomes Project (http://www.nitrc.org/frs/?group_id=296). The dataset included 26 healthy controls (13 males/13 females) aged between 23 and 44 years (mean = 29.77 ± 5.21 years). The resting-state functional MRIs were acquired on a 3 T Trio Tim Siemens Magnetom (Siemens). The scanning protocol was as follows: repeat time = 2300 ms, echo time = 30 ms, time points = 195, slice number = 34, flip angle = 90°, voxel size = 3 × 3 × 4 mm^3, field of view = 192 × 192.

PET image preprocessing

The ^{18}F-AV-1451 PET scans were preprocessed using Statistical Parametric Mapping (SPM) version 8 (Wellcome Trust Centre for Neuroimaging, Institute of Neurology, University College London). The images were spatially normalized to a tau template of a healthy control group. This template was previously established by our group based on a dataset of ^{18}F-AV-1451 PET scans from 19 healthy controls (mean age = 56.63 ± 16.65 years) provided by Avid Radiopharmaceuticals (Bischof *et al.*, 2016; Hammes *et al.*, 2017). The normalized PET scans were smoothed using a Gaussian filter of 12 mm full-width at half-maximum. Using the whole cerebellum as reference region, standard uptake value ratio (SUVR) images were computed utilizing in-house scripts in MATLAB R2016a (The MathWorks, Inc., Natick, MA, USA). To assess specific Alzheimer's disease-related tau pathology patterns, images were z-transformed using the mean and deviation image from a healthy control sample. A detailed description of the sample and z-transformation can be found elsewhere (Bischof *et al.*, 2016). The generated z-transformed images were then subjected to an ICA.

Resting-state functional MRI image preprocessing

The resting-state functional MRI dataset was preprocessed using the pipeline of the Data Processing Assistant for Resting-State functional MRI (DPARSF) toolbox, version 4.3 (Yan and Zang, 2010). The pipeline consists of the following steps: initially, the first 10 time points of each subject were removed and the remaining slices were processed with slice timing. Second, nuisance variables were regressed including white matter, CSF, and global mean signal. To control for head motion, the Friston 24 parameter model was applied (Friston *et al.*, 1996). Third, the realigned images were normalized to the default EPI template provided by the DPARSF toolbox. In a final step, the images were smoothed with a Gaussian filter of 8 mm. All preprocessed images were visually checked to assure that the normalization process had not resulted in distorted images. The preprocessed images were then used for the seed-based functional connectivity analysis.

Statistical analysis

Independent component analysis

To identify independently coherent TPNs, we performed an ICA on the z-standardized tau-PET images using the group ICA function of the functional MRI Toolbox (GIFT toolbox, version 4.0a, 2015; MIALAB, The Mind Research Network, University of New Mexico, Albuquerque, NM, USA). To avoid overfitting of the data based on the given number of input images and to create meaningful orthogonal components, the default setting of 20 components was reduced to 10 components (Särelä and Vigário, 2003). We then applied the *Infomax* algorithm implemented in the GIFT toolbox to extract common tau pathology features from the PET dataset.

To support our ICA approach and to evaluate the possible influence of confounding factors that might bias the results, we performed a series of additional analyses: we ran the ICA with different numbers of allowed components (five and 20 components), with a different Gaussian kernel (8 mm instead of 12 mm), and, in addition, an ICA including only scans from patients who were amyloid-positive on their amyloid PET scan ($n = 16$). Moreover, we conducted a conventional SPM *t*-test to identify peaks of tau pathology. For this, we compared the Alzheimer's disease group against a group of healthy controls ($n = 19$) using a voxel-based independent *t*-test. The identified peaks of tau pathology were used as seeds in a following seed-based functional MRI analysis.

Seed-based functional connectivity analysis

To assess if regions of high tau burden are involved in functional connectivity networks, we conducted a seed-based analysis using the preprocessed resting-state functional MRI dataset by Berlin-Margulies (Rohr *et al.*, 2013). As seeds for the functional connectivity analysis, we extracted the coordinate of the maximal peak z-score from each generated TPN. The seeds of maximum tau burden were each defined as a sphere centred at the respective peak coordinate with a radius of 5 mm. Given that we allowed 10 components to be generated by the ICA, we obtained 10 tau-dependent seeds, which were submitted to the functional connectivity analysis using the DPARSF toolbox.

Following the pipeline of the DPARSF toolbox for the functional connectivity analysis, the motion parameters, white matter, CSF, and global mean signal were regressed out. Next, the images were band-pass filtered at 0.01–0.1 Hz. To reduce the number of comparisons for the connectivity analysis conducted in SPM 12, we included a grey matter mask. Then, the correlation of the resting-state functional MRI time series between the respective seed and coherently active regions were computed for each subject yielding individual functional connectivity maps for each seed. In a last step, we conducted one-sample *t*-tests in SPM 12 (family-wise error, $P < 0.05$) comprising the individual functional connectivity maps for each seed. Age and gender were included as covariates. The SPM analyses yielded the respective functional connectivity maps for each seed.

Evaluation of spatial overlap: Dice similarity coefficient

To examine the overlap between the TPNs and the corresponding tau-dependent seed-based networks, we next calculated the Dice similarity coefficient (DSC). The DSC is a measure that quantifies the spatial overlap between two binarized maps and is calculated as follows:

$$\mathrm{DSC} = \frac{2n_t}{(n_x + n_y)} \quad (1)$$

where n_t denotes the volume intersection between the image volume n_x and n_y, which is divided by the sum of the respective image volumes n_x and n_y. The DSC thereby yields the percentage-wise overlap between two maps/networks. It is interpreted as follows: <0.2 reflects poor, 0.2–0.4 fair, 0.4–0.6 moderate, 0.6–0.8 good, and >0.8 near complete overlap (Savio *et al.*, 2017).

To calculate the DSC, we first binarized the generated *t*-maps of the seed-based networks. Next, the generated TPNs were binarized at a z-score of $z > 2.0$. We then compared the spatial overlap between the TPNs and the corresponding seed-based networks. Furthermore, to characterize the topography of the seed-based networks, we compared these networks with previously established functional connectivity networks obtained by a resting-state functional MRI study in 27 healthy subjects at the FIND lab of Stanford University (Shirer *et al.*, 2012). The Stanford networks consist of 14 networks, including the DMN, salience network and language network, and have consistently been used by other studies to characterize resting-state functional connectivity networks (Lehmann *et al.*, 2013; Leonardi *et al.*, 2014; Lim *et al.*, 2014). We quantitatively compared the spatial overlap of each binarized seed-based network against all binarized resting-state networks. The resting-state network with the highest dice coefficient was chosen as best match for the seed-based network.

Relation between Braak stages and tau pathology networks

To examine the association between tau pathology in the respective TPNs and the individual Braak stage of each patient, we extracted mean SUVRs for Braak stages I/II–VI for each patient based on the region of interest-based Braak staging approach previously used (Schöll *et al.*, 2016; Hoenig *et al.*, 2017). Moreover, we computed the median SUVR for each Braak stage across the patient sample. Patients, who had a mean SUVR greater than the median, were determined to be

positive for the respective Braak stage, whereas patients who had a lower SUVR than the median were classified as negative. The highest positive Braak stage was used for final classification. Patients could obtain a score ranging from 2–6 (corresponding to Braak stage I/II–VI) and were grouped into either an early Braak (score 2–3) or advanced Braak group (stage 4–6). Finally, we compared the mean SUVRs of each TPN between the early ($n = 10$) and the advanced ($n = 12$) Braak group. We extracted the mean SUVRs for the respective components based on the intensity standardized images using the binarized component maps. As the assumptions for normality and homoscedasticity were not given, the Mann-Whitney U-test was used for comparison. Results were corrected for multiple comparison using Bonferroni correction ($^*P = 0.005$).

Relation between cognitive function and tau burden in tau pathology networks

We further examined whether tau burden within distinct TPNs was associated with global cognitive dysfunction. We used the

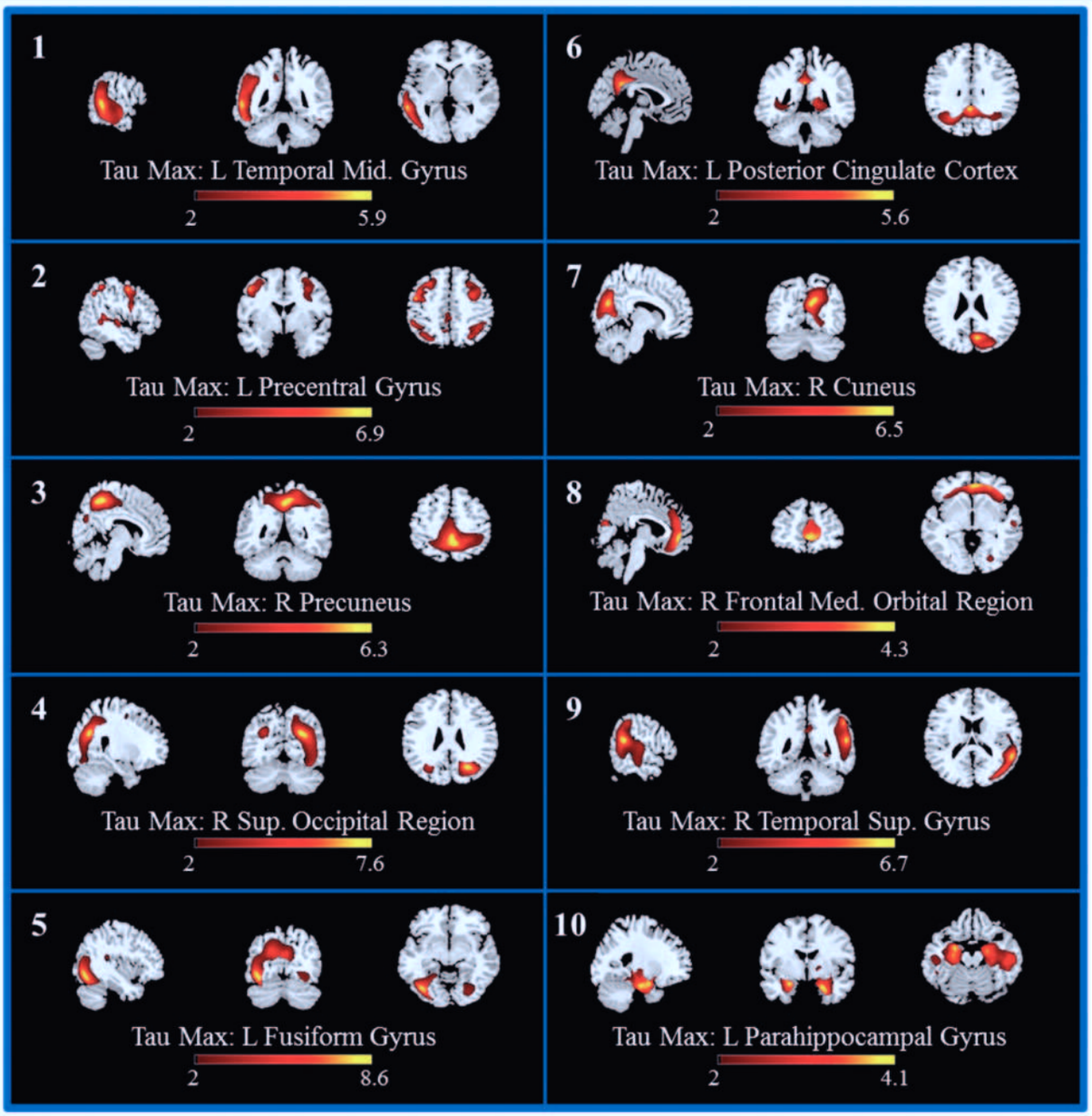

Figure 1 Illustration of independently coherent tau pathology networks. The respective region corresponding to the peak coordinates of each component and the z-score range are depicted below each component. The components are projected on the Colin brain in MNI space. Max = maximum; Med. = medial; Mid. = middle; Sup. = superior.

Table 2 Tau load of independent tau pathology networks

TPN	Mean SUVR (SE)
1	1.70 (0.09)
2	1.66 (0.11)
3	1.57 (0.12)
4	1.68 (0.90)
5	1.52 (0.08)
6	1.71 (0.10)
7	1.38 (0.07)
8	1.42 (0.07)
9	1.59 (0.09)
10	1.51 (0.04)

Mean SUVR and standard error (SE) for each tau pathology network are provided.

MMSE as a measure of global cognitive function (Folstein *et al.*, 1975). Both tau burden within each component and global cortical tau were quantified based on the individual SUVR images using the binarized component maps and a whole-brain cortical grey matter region of interest, respectively. The extracted SUVRs for each component and for global cortical tau burden of each patient were correlated with the individual MMSE scores including age and gender as covariates. The analyses were corrected for multiple comparisons using Bonferroni correction ($^*P = 0.0045$).

Results

Tau pathology networks

The ICA resulted in the detection of independent TPNs, which spatially resembled established language, frontal control, default mode, visuospatial, and hippocampal networks (Fig. 1). Some of the TPNs showed a symmetrical bi-hemispheric expansion (Components 2–4, 6, 8 and 10), whereas the remaining components were lateralized (Components 1, 5, 7 and 9). Moreover, the TPNs were characterized by varying loads of tau pathology (Table 2). The generated TPNs coincided with highly functionally connected regions predominantly involving parietal and temporal areas. The total per cent variance explained by all 10 components was 95.7%. The topographical distributions of the TPNs are depicted in blue in Fig. 3.

The different ICA settings revealed similar components confirming the statistical stability of the generated TPNs. Importantly, the ICA including only amyloid-positive patients resulted in similar components as the initial ICA (Supplementary Fig. 4). Moreover, the conventional SPM approach using a *t*-test yielded four peaks of tau pathology, which resembled the tau maxima detected by the ICA (Supplementary Table 1). Further details of the additional analyses can be found in the Supplementary material.

Table 3 Coordinates and z-scores of the tau pathology networks

TPN	Max z-score	Coordinates			AAL region
		x	*y*	*z*	
1	5.54	−60	−46	0	L temporal middle gyrus (85)
2	6.53	−48	0	46	L precentral gyrus (1)
3	5.95	8	−52	52	R precuneus (68)
4	7.11	28	−68	26	R superior occipital region (50)
5	8.06	−40	−66	−12	L fusiform gyrus (55)
6	5.10	0	−46	28	L posterior cingulate cortex (35)
7	5.32	10	−72	24	R cuneus (46)
8	3.96	6	50	−6	R frontal medial orbital region (26)
9	6.32	58	−48	16	R superior temporal gyrus (82)
10	3.93	−24	−5	−22	L parahippocampal gyrus (39)

The maximum z-score and the peak coordinates of each tau pathology network with the corresponding brain region based on the automated anatomical labelling atlas are listed (Tzourio-Mazoyer *et al.*, 2002). AAL = automated anatomical labelling atlas; L = left; R = right.

Tau-dependent seed-based functional networks

The tau maxima of the respective TPNs used for the seed-based approach corresponded to the following regions: temporal middle gyrus, precentral gyrus, precuneus, superior occipital region, fusiform gyrus, posterior cingulate cortex, cuneus, frontal medial orbital region, superior temporal gyrus and parahippocampal gyrus (Table 3). The seed-based functional connectivity analysis resulted in specific functional connectivity networks for each tau maxima. For several seed-based analyses, the functional networks included remote brain regions, which were not anatomically adjacent to the corresponding seed region (seed-based networks: 1, 2, 6, 8, 9, and 10). Furthermore, the tau-dependent seed-based networks were characterized by a symmetrical bi-hemispheric functional connectivity pattern. The respective projections of the seed-based networks are depicted in red in Fig. 3.

Spatial overlap between distribution of tau pathology and functional networks

The comparison between the identified TPNs and the tau-dependent seed-based functional connectivity networks yielded moderate spatial overlap (DSC: 0.4–0.6) for Components 3, 5 and 10 with their corresponding tau-dependent seed-based functional networks. In addition, TPN Components 1, 4, 7, 8 and 9 were fairly (DSC: 0.2–0.4) associated with the corresponding tau-maximum seeded functional network. Only poor overlap (DSC < 0.2) was found between the seed-based networks and the remaining components (Components 2 and 6). The respective DSCs are reported in Table 4.

The comparison between the tau-dependent seed-based networks with known resting-state functional connectivity

Table 4 Dice similarity coefficient for the overlap between networks

DSC for overlap between TPN and SBN		DSC for overlap between SBN and RSN	
TPN 1 and SBN 1	0.39	SBN 1 and language network	0.37
TPN 2 and SBN 2	0.17	SBN 2 and salience network	0.28
TPN 3 and SBN 3	0.57	SBN 3 and ventral DMN	0.56
TPN 4 and SBN 4	0.34	SBN 4 and ventral DMN	0.42
TPN 5 and SBN 5	0.41	SBN 5 and higher visual network	0.33
TPN 6 and SBN 6	0.13	SBN 6 and dorsal DMN	0.51
TPN 7 and SBN 7	0.36	SBN 7 and primary visual network	0.23
TPN 8 and SBN 8	0.25	SBN 8 and dorsal DMN	0.55
TPN 9 and SBN 9	0.38	SBN 9 and language network	0.52
TPN 10 and SBN 10	0.46	SBN 10 and hippocampal network	na

The table summarizes the quantification of the overlap between the tau pathology network and the corresponding seed-based network and the seed-based network and best-matching Stanford resting-state network. na = not available; RSN = resting-state network; SBN = seed-based network.

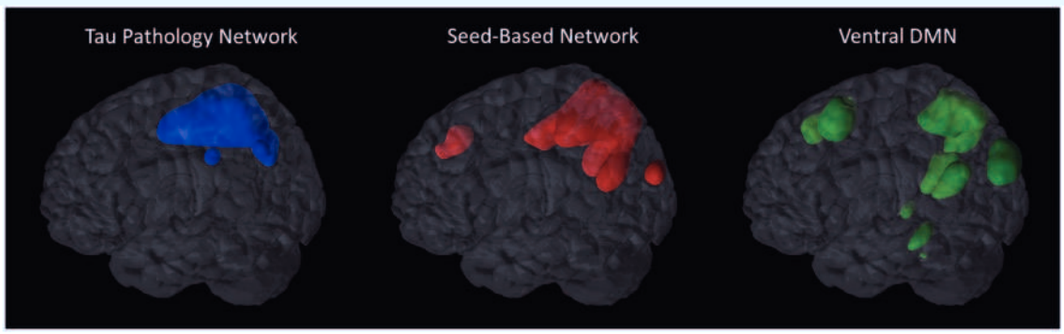

Figure 2 Exemplary illustration of the distribution pattern of respective networks. The networks are rendered on the inflated Colin brain in MNI space. Blue = TPN; Red = seed-based network; Green = ventral DMN.

networks yielded moderate overlap (DSC: 0.4–0.6) for seed-based networks 3, 4, 6, 8 and 9, predominantly with regions associated with the ventral and dorsal DMN. Moreover, fair overlap (DSC: 0.2–0.4) was observed between the seed-based networks 1, 2, 5 and 7 and the language, the salience, higher visual, and primary visual network. The seed-based network 10 strongly resembled the hippocampal network. As the hippocampal network is not part of the predefined Stanford networks, we could not quantitatively assess the actual spatial overlap. The respective DSCs are reported in Table 4.

Figure 2 provides an exemplary illustration of the best overlapping TPN, the corresponding seed-based network, and the best matching Stanford resting-state network on a rendered brain surface. Figure 3 illustrates the spatial resemblance between the respective components (highlighted in blue) and the corresponding seed-based network (highlighted in red) and the best-matching Stanford resting-state network (highlighted in green), respectively. This figure further includes the DSCs for the quantification of the spatial overlap between the respective TPNs and the seed-based networks (first DSC) and between each seed-based network and the corresponding Stanford resting-state network (second DSC).

Relationship between Braak stages and tau pathology networks

The advanced Braak group showed significantly higher SUVRs in eight components when compared to the early Braak group (Fig. 4). Mean SUVRs in Components 3 and 7 did not significantly differ between groups after correcting for multiple comparison ($^*P = 0.005$), although a trend was observed. A summary of the U-statistics can be found in Supplementary Table 2.

Cognitive function and tau burden in distinct tau pathology networks

Global cognitive function was negatively correlated with tau burden in Components 4 [$r(18) = -0.496$, $P = 0.026$], 5 [$r(18) = -0.554$, $P = 0.011$], and 7 [$r(18) = -0.641$, $P = 0.002$]. A trend significant effect was observed for global cognitive function and Component 3 [$r(18) = -0.440$, $P = 0.052$]. Global cortical tau burden, assessed based on a cortical grey matter region of interest, was not negatively correlated with global cognitive function [$r(18) = -0.305$, $P = 0.190$]. Exclusively, the negative association between global cognitive function and tau burden in Component 7 survived correction for multiple comparison

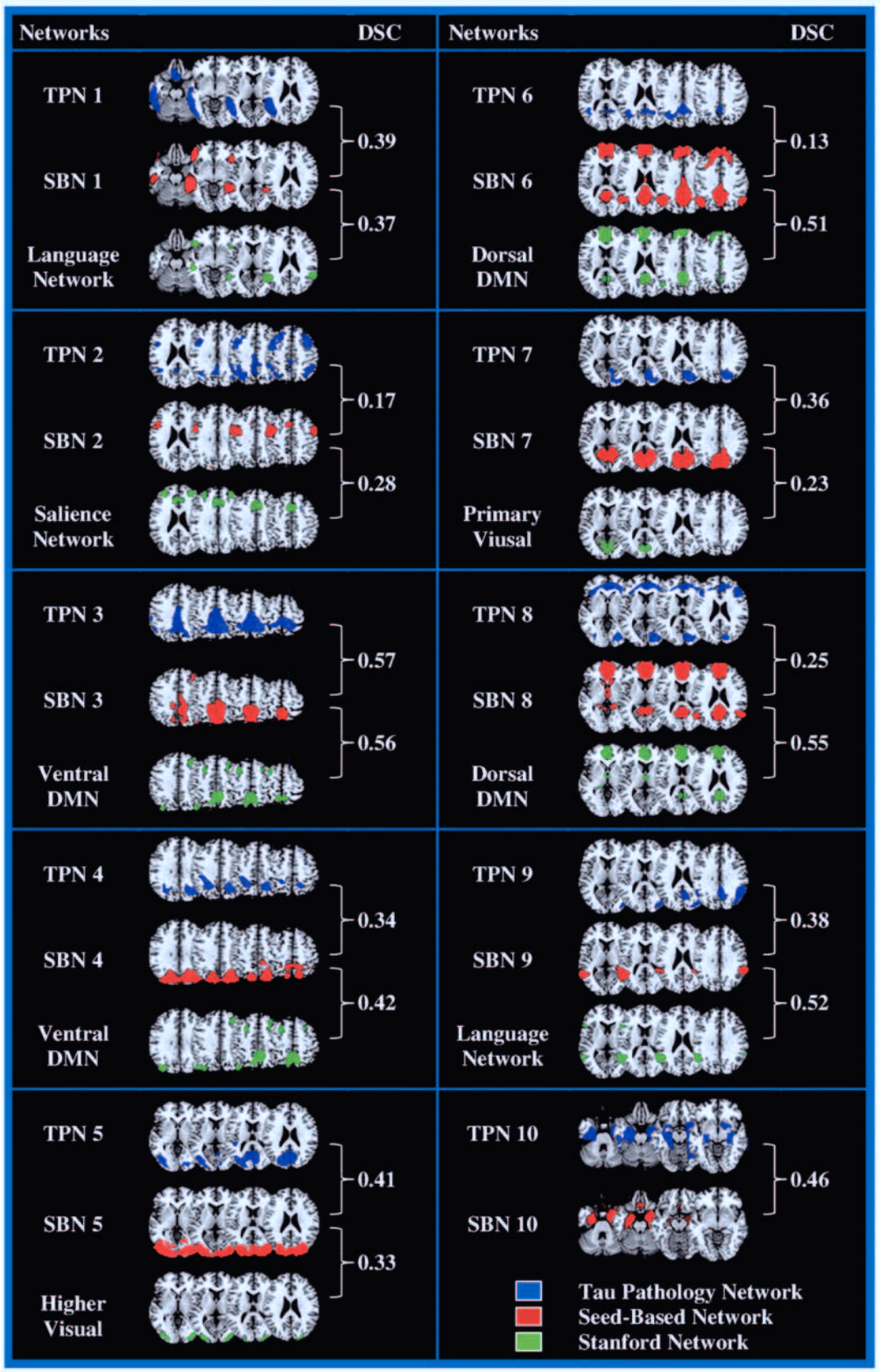

Figure 3 Illustration of networks and corresponding dice similarity coefficient. The respective tau pathology networks are illustrated in blue, the corresponding seed-based networks in red, and the best-matching resting-state Stanford network in green. The first DSC per cell represents the spatial overlap between the TPN and the seed-based network, the second coefficient relates to the overlap between the seed-based and the resting- state Stanford network. All networks are projected on the Colin brain in MNI space. SBN = seed-based network.

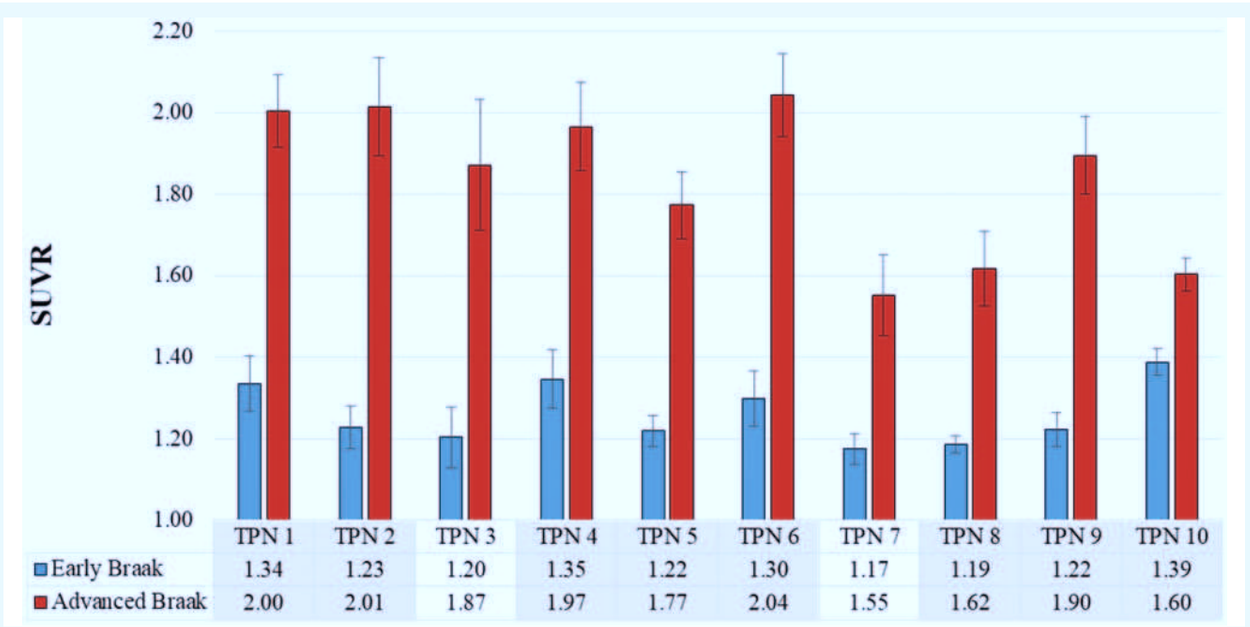

Figure 4 Illustration of tau burden in each independent component for the early and advanced Braak group. Mean SUVRs and standard error for each component are depicted for the early Braak (blue) and advanced Braak (red) group. Significant differences between groups that survived the multiple comparison correction are highlighted in grey.

(*P = 0.0045). The tau maximum of Component 7 coincided with cuneal regions, whereas the tau maximum of Component 3 was located in precuneal areas, of Component 4 in superior occipital, and of Component 5 in fusiform gyral areas.

Discussion

In the current study, we identified a set of independently coherent networks of tau pathology in a sample of patients with mild-to-moderate Alzheimer's disease. This finding supports the idea that the aggregation of tau pathology in the brain follows several independent pathways and partly develops coherently in different compartments of the brain. The peaks of tau within these detected TPNs included, among others, the precuneus, parahippocampus, and posterior cingulate cortex, regions known to be involved in various functional networks. In accordance with this, the TPNs overlapped distinctly with seed-based functional connectivity networks, some of which have previously been reported to be impaired in Alzheimer's disease, including the DMN (Greicius *et al.*, 2004; Zhang *et al.*, 2010; Zhou *et al.*, 2010) and the frontal control network (Agosta *et al.*, 2012; Lehmann *et al.*, 2013; Balthazar *et al.*, 2014). Moreover, tau burden within the TPNs was associated with the advancement along Braak stages and global cognitive dysfunction, indicating that the identified networks may bear clinical relevance. In the following, we discuss our findings in the context of (i) distribution of tau pathology along independent pathways; (ii) the relevance of TPNs in regard to disease progression and cognitive profiles; and (iii) the relationship of these TPNs with functional connectivity networks.

Properties of independent tau pathology networks

Here, we determined a set of distinct TPNs by means of ICA. Some of the TPNs involved regions that were not anatomically adjacent. This is *per se* of interest as it indicates that tau pathology does not distribute homogenously across the brain, but importantly propagates across independent pathways and possibly arises synchronously in different brain compartments at certain stages of the disease.

Interestingly, several TPNs were characterized by a symmetrical distribution pattern across hemispheres, whereas some were asymmetric. This characteristic difference in the symmetry of the TPNs may be partly attributed to early disease stage, where tau pathology may not have advanced to a symmetric pattern across hemispheres within a given network, but has centred on the most susceptible regions of tau accumulation. Indeed, according to recent models of tau propagation misfolded tau proteins predominantly spread along the most interconnected regions of the seed of tau pathology (Fox *et al.*, 2011; Liu *et al.*, 2012; Menkes-Caspi *et al.*, 2015). Thus, depending on the stage of the disease and the anatomical location of the seed of pathology, which may be represented by the tau maxima of each independent component, tau distribution

patterns may differ in their symmetry. Moreover, the current finding of asymmetric components accords with the known fact that neurodegenerative disorders may start in one hemisphere and initially spread dominantly across this hemisphere before eventually affecting the other hemisphere in later stages of disease (Shi *et al.*, 2009; Claassen *et al.*, 2016). In this regard, the implications of using ICA as an analysis method also need to be considered. ICA is a data-driven approach that is based on the underlying tau pathology distribution of the patient sample, which in this study consists of patients with mild-to-moderate Alzheimer's disease. Consequently, component patterns of coherent tau pathology can be identified that may be characterized either by an asymmetric distribution pattern, likely reflecting earlier stages of the disease, or by symmetric and bihemispheric patterns, potentially reflecting a more advanced disease stage. ICA hence defines independent regional patterns of coherent tau pathology, which do not necessarily have to be symmetric supporting the current finding of asymmetric and symmetric component patterns.

As discussed above, ICA can determine unique disease-specific and coherent patterns of tau pathology without any *a priori* knowledge or topographic assumptions (Pagani *et al.*, 2016). This blind source separation technique contrasts conventional voxel-based statistical parametric mapping approaches that are often based on *a priori* hypotheses regarding the cortical disease localization and require categorical distinction into significant and non-significant voxels depending on the intensity values of the voxels. ICA, in contrast, provides a more graduated consideration, where significance is not based on severity but regional coherence of pathology and thus regional interrelations. Importantly, ICA does thereby not exclusively provide components of highest tau pathology, but can also determine regional distribution patterns of lower pathology load, which are nevertheless characterized by synchronous tau pathology aggregation. In compliance with this, in the current study the conventional SPM approach only yielded four peaks of tau pathology, whereas by means of ICA several additional TPNs were established. Importantly, the TPNs identified by ICA were characterized by varying loads of tau pathology pointing towards different susceptibility of these TPNs potentially depending on the stage of the disease. Intriguingly, the components involving orbitofrontal and cuneal areas showed lowest tau burden. These regions are known to be affected relatively late in Alzheimer's disease according to the neuropathological Braak stages (Braak and Braak, 1991, 1995). Interestingly, when directly assessing the relationship between the neuropathological Braak stages and the identified TPNs, we observed that individuals in an advanced Braak stage demonstrated higher tau pathology burden in the established TPNs as compared to individuals at an earlier Braak stage. This result indicates that the accumulation of tau pathology within the identified TPNs may contribute to the advancement along Braak stages. Moreover, in the early Braak stage group highest tau burden was observed in the TPN associated with the parahippocampus, whereas the advanced Braak stage group presented highest tau pathology in the TPN associated with the posterior cingulate cortex. This may suggest that distinct TPNs exist as a determinant of each Braak stage. Larger data samples of early and advanced Braak stage groups will be required to investigate this assumption further. Overall, the current findings suggest that the differential load of tau pathology in the independent TPNs may track the expansion of tau pathology at various disease stages.

In addition to the implications of the TPNs with respect to the neuropathological Braak staging, tau pathology within the TPN including cuneal and primary visual areas was also associated with decreased global cognitive function. This finding points towards a specific deleterious effect as soon as tau pathology strikes visual cortical brain regions (Braak and Braak, 1991, 1995) underscoring the regional specificity of a tau-cognition relationship. Moreover, these findings are consistent with recent findings reporting a relationship between cognitive function and regional tau pathology (Brier *et al.*, 2016; Ossenkoppele *et al.*, 2016; Shimada *et al.*, 2017). To achieve a more fine-grained characterization of distinct cognitive profiles in Alzheimer's disease, future studies may employ an elaborate neuropsychological assessment and examine its correspondence with the TPNs identified here. Alternatively, as atypical cases of Alzheimer's disease such as posterior cortical atrophy or the logopenic variant of Alzheimer's disease express distinct cognitive profiles, which are dissociable from amnestic cases, further investigations are warranted that explore whether these clinical variants are also characterized by variant-specific TPNs.

Overall, our results provide first evidence of independently coherent tau pathology networks, which not only appear to track disease progression but also, at least in part, relate to global cognitive dysfunction. Importantly, these networks of interrelated tau deposition point towards brain regions potentially being synchronously affected by tau pathology during the course of the disease, providing new insights into the mechanistic pathway of the disease. Given that the identified TPNs differed in their topographical distribution and in the degree of tau pathology, it will be of great interest to investigate the influence of additional factors on the generation of these networks. In particular, a putative synergistic effect of amyloid-β and tau pathology may be of interest with regard to the propagation of tau pathology along the identified networks. Moreover, investigating how the cellular, functional, and structural composition underlying specific networks influences the propagation of tau pathology and thereby the generation of these distinct TPNs will provide further information on the pathophysiological processes underlying Alzheimer's disease.

Relation between independent tau pathology patterns and functional connectivity networks

Some of the identified TPNs involved anatomically distant regions, indicating that these regions may share a joint mechanism, which could be of structural or functional nature and which may contribute to the coherent accumulation of tau pathology in these compartments. In the current study, we focused on the role of seeded functional connectivity in regard to *in vivo* tau distribution patterns for two reasons. First, seed-based connectivity networks include regions that show highest connectivity to the seed and thus comply with recent models of tau propagation. Second, functional connectivity hubs have been suggested to be most susceptible to the development of neuropathology (Buckner *et al.*, 2009; Drzezga *et al.*, 2011; de Haan *et al.*, 2012). From these hubs pathology may then spread to connected brain regions (Buckner *et al.*, 2009; Drzezga *et al.*, 2011; de Haan *et al.*, 2012). Indeed, a number of studies consistently demonstrated striking similarity and overlap of amyloid-β plaque pathology with functional connectivity networks (Buckner *et al.*, 2005, 2009; Lehmann *et al.*, 2013; Grothe and Teipel, 2016). In accordance with this, we observed tau-dependent seed-based functional networks, characterized by a symmetrical bihemispheric activation, which in part spatially corresponded to the established TPNs.

Some of the seed-based networks resembled the salience, the primary visual, the higher visual, the language, and the hippocampal network indicating that tau pathology does not exclusively distribute along one particular network. This finding is in accordance with recently provided evidence demonstrating that the Alzheimer's disease-associated tau pathology pattern corresponds to several cognition-relevant networks (Hansson *et al.*, 2017). Interestingly, the majority of tau-dependent seed-based networks established in the current study predominantly overlapped with regions of the ventral and dorsal DMN. This suggests that the DMN may be particularly susceptible to not only amyloid-β pathology, as previously shown (Buckner *et al.*, 2005, 2009; Grothe and Teipel, 2016), but also to tau pathology. Note, however, that all identified seed-based networks overlapping with the DMN had different origins, suggesting that the networks identified in our study may represent subnetworks of a more superordinate network. The existence of such subnetworks within a superordinate network has been recently proposed (Doucet *et al.*, 2011). These subnetworks may differently be affected depending on the stage of the disease and therefore, by using ICA, several components, each with a different pathological load, can actually belong to a more superordinate network. Thus, directly comparing the spatial overlap between ICA-derived patterns of tau load and an entire resting-state network such as the DMN may not be an appropriate comparison, as the ICA patterns may only reflect subnetworks of the resting-state networks. Therefore, generating seed-based functional connectivity networks from the ICA-derived patterns likely allows us to more accurately compare the functional networks related to tau pathology distribution patterns.

Although we observed an overlap between the TPNs, the tau-dependent seed-based networks, and known resting-state networks, the overlap was moderate. Several aspects may contribute to this moderate spatial correspondence. As the seed-based functional connectivity networks in the current study were defined based on a group of healthy young adults, they likely differed from the functional networks present in Alzheimer's disease patients (Jones *et al.*, 2016; Teipel *et al.*, 2016). Following the concept of tau propagation, tau pathology may no longer be able to expand along these networks due to disease-related disconnection between regions within a given network, changes in the location of network hubs, or functional breakdown of the entire network. Thus, the overlap between the tau-dependent seed-based networks and the TPNs may have been moderate due to disease-related and/or age-related changes in network architecture. Based on the proposed prion-like mechanisms of tau, tau pathology may propagate along reorganized networks that may differ from the ones identified in the young.

Furthermore, although a close link between structural and resting-state functional connectivity has been reported (Greicius *et al.*, 2009), functional connectivity maps only capture the superficial structure of regions and collapse several subregions into one. Given that tau pathology appears to follow synaptic connectivity (Clavaguera *et al.*, 2009; de Calignon *et al.*, 2012; Liu *et al.*, 2012), the spreading pattern may depend on structural connectivity rather than functional connectivity. It is thus possible that the overlap between structural networks and the established TPNs is more coherent. Future multimodal studies using diffusion tensor imaging and functional MRI are warranted to understand the structural and functional underpinnings contributing to the propagation of misfolded tau proteins within neuronal networks.

Finally, we only included patients with mild-to-moderate Alzheimer's disease in our current analyses. Thus, tau pathology in the current patient cohort may just have started to spread from the initial seed, thereby rendering the overlap with the corresponding seed-based network rather moderate. Longitudinal studies are necessary to assess whether at advanced stages of Alzheimer's disease, the overlap between the TPNs and the corresponding seed-based networks becomes more concordant.

Despite these arguments, it appears that the functional connections between regions, which are characterized by synchronous oscillatory activity, may provide a pathway contributing to the propagation of tau pathology within distinct neural networks. Longitudinal tau-PET and functional imaging data from the same Alzheimer's disease cohort will be necessary to establish whether the functional coherence between regions acts as an amplifying mechanism for tau pathology to spread.

Limitations

A few limitations need to be considered when interpreting our results. First, our analysis was restricted to a relatively small PET dataset. Studies that include larger patient cohorts are needed to confirm that the established TPNs are characteristic for Alzheimer's disease patients. Second, it has to be noted that we used a resting-state functional MRI dataset of young healthy controls, which was used to establish seed-based functional networks associated with the healthy state. Using a resting-state functional MRI dataset of age-matched healthy older controls would have allowed us to investigate the possible age-related pattern of tau distribution along neural networks. However, including an age-matched control sample would have required additional PET or CSF measurements to exclude any existing ageing-related pathology, which may have already affected (subclinically) network structures. Moreover, we cannot exclude spill-over effects from the choroid plexus influencing the signal in hippocampal regions. However, given that only one component was associated with hippocampal regions, we believe that the potential influence was marginal at most. Finally, we used a cross-sectional approach to assess the existence of TPNs and their relation to functional networks. Longitudinal designs may be better suited to explore the temporal spread of tau pathology along functionally connected brain regions.

Conclusion

The results of this study indicate that in Alzheimer's disease, the spatial distribution of tau pathology is not homogeneous but seems to progress within independent, coherent networks. Moreover, tau pathology load in these identified networks is associated with the advancement along Braak stages. In addition, the independent, coherent networks were characterized by differential distribution patterns, which in turn partially corresponded with functional connectivity networks. The relationship between functional connectivity network and TPNs may offer new insights into the possible mechanism of tau propagation across brain regions. Longitudinal approaches are warranted to further elucidate the temporal spreading pattern of tau pathology across large-scale networks, which will provide important information on the mechanisms underlying Alzheimer's disease and may further inform investigation of anti-tau based treatment efficacy.

Acknowledgements

We thank AVID Radiopharmaceuticals for providing us with their dataset of healthy controls scanned using the ^{18}F-AV-1451 tracer.

Funding

This study was supported by funding from the Deutsche Forschungsgemeinschaft (DR 445/9-1). G.R.F. and J.K. are grateful for the support by the Marga and Walter Boll Foundation, Kerpen, Germany. A.D., J.K. and O.A.O. thank the Brandau-Laibach-Foundation, Cologne, Germany, for additional support.

Supplementary material

Supplementary material is available at *Brain* online.

References

Agosta F, Pievani M, Geroldi C, Copetti M, Frisoni GB, Filippi M, Resting state fMRI in Alzheimer's disease: beyond the default mode network. Neurobiol Aging 2012; 33: 1564–78.

Balthazar ML, Pereira FR, Lopes TM, da Silva EL, Coan AC, Campos BM, et al. Neuropsychiatric symptoms in Alzheimer's disease are related to functional connectivity alterations in the salience network. Hum Brain Mapp 2014; 35: 1237–46.

Bischof GN, Jessen F, Fliessbach K, Dronse J, Hammes J, Neumaier B, et al. Impact of tau and amyloid burden on glucose metabolism in Alzheimer's disease. Ann Clin Transl Neurol 2016; 3: 934–9.

Braak H, Braak E. Neuropathological stageing of Alzheimer-related changes. Acta Neuropathol 1991; 82: 239–59.

Braak H, Braak E. Staging of Alzheimer's disease-related neurofibrillary changes. Neurobiol Aging 1995; 16: 271–8.

Brier MR, Gordon B, Friedrichsen K, McCarthy J, Stern A, Christensen J, et al. Tau and Aβ imaging, CSF measures, and cognition in Alzheimer's disease. Sci Transl Med 2016; 8: 338ra66–ra66.

Buckner RL, Sepulcre J, Talukdar T, Krienen FM, Liu H, Hedden T, et al. Cortical hubs revealed by intrinsic functional connectivity: mapping, assessment of stability, and relation to Alzheimer's disease. J Neurosci 2009; 29: 1860–73.

Buckner RL, Snyder AZ, Shannon BJ, LaRossa G, Sachs R, Fotenos AF, et al. Molecular, structural, and functional characterization of Alzheimer's disease: evidence for a relationship between default activity, amyloid, and memory. J Neurosci 2005; 25: 7709–17.

Calhoun VD, Adali T. Multisubject independent component analysis of fMRI: a decade of intrinsic networks, default mode, and neurodiagnostic discovery. IEEE Rev Biomed Eng 2012; 5: 60–73.

Claassen DO, McDonell KE, Donahue M, Rawal S, Wylie SA, Neimat JS, et al. Cortical asymmetry in Parkinson's disease: early susceptibility of the left hemisphere. Brain Behav 2016; 6: e00573.

Clavaguera F, Bolmont T, Crowther RA, Abramowski D, Frank S, Probst A, et al. Transmission and spreading of tauopathy in transgenic mouse brain. Nat Cell Biol 2009; 11: 909–13.

Cohen AL, Fair DA, Dosenbach NU, Miezin FM, Dierker D, Van Essen DC, et al. Defining functional areas in individual human brains using resting functional connectivity MRI. Neuroimage 2008; 41: 45–57.

de Calignon A, Polydoro M, Suárez-Calvet M, William C, Adamowicz DH, Kopeikina KJ, et al. Propagation of tau pathology in a model of early Alzheimer's disease. Neuron 2012; 73: 685–97.

de Haan W, Mott K, van Straaten EC, Scheltens P, Stam CJ. Activity dependent degeneration explains hub vulnerability in Alzheimer's disease. PLoS Comput Biol 2012; 8: e1002582.

Di X, Biswal BB, Alzheimer's Disease Neuroimaging Initiative. Metabolic brain covariant networks as revealed by FDG-PET with reference to resting-state fMRI networks. Brain Connect 2012; 2: 275–83.

Doucet G, Naveau M, Petit L, Delcroix N, Zago L, Crivello F, et al. Brain activity at rest: a multiscale hierarchical functional organization. J Neurophysiol 2011; 105: 2753–63.

Dronse J, Fliessbach K, Bischof GN, von Reutern B, Faber J, Hammes J, et al. *In vivo* patterns of Tau pathology, Amyloid-β burden, and neuronal dysfunction in clinical variants of Alzheimer's disease. J Alzheimers Dis 2017; 55: 465–71.

Drzezga A, Becker JA, Van Dijk KR, Sreenivasan A, Talukdar T, Sullivan C, et al. Neuronal dysfunction and disconnection of cortical hubs in non-demented subjects with elevated amyloid burden. Brain 2011; 134: 1635–46.

Fan Y, Resnick SM, Wu X, Davatzikos C. Structural and functional biomarkers of prodromal Alzheimer's disease: a high-dimensional pattern classification study. Neuroimage 2008; 41: 277–85.

Folstein MF, Folstein SE, McHugh PR. "Mini-mental state": a practical method for grading the cognitive state of patients for the clinician. J Psychiatr Res 1975; 12: 189–98.

Fox LM, William CM, Adamowicz DH, Pitstick R, Carlson GA, Spires-Jones TL, et al. Soluble tau species, not neurofibrillary aggregates, disrupt neural system integration in a tau transgenic model. J Neuropathol Exp Neurol 2011; 70: 588–95.

Friston KJ, Williams S, Howard R, Frackowiak RS, Turner R. Movement-related effects in fMRI time-series. Magn Res Med 1996; 35: 346–55.

Greicius MD, Srivastava G, Reiss AL, Menon V. Default-mode network activity distinguishes Alzheimer's disease from healthy aging: evidence from functional MRI. Proc Natl Acad Sci USA 2004; 101: 4637–42.

Greicius MD, Supekar K, Menon V, Dougherty RF. Resting-state functional connectivity reflects structural connectivity in the default mode network. Cereb Cortex 2009; 19: 72–8.

Grothe MJ, Teipel SJ. Spatial patterns of atrophy, hypometabolism, and amyloid deposition in Alzheimer's disease correspond to dissociable functional brain networks. Hum Brain Mapp 2016; 37: 35–53.

Hammes J, Bischof GN, Giehl K, Faber J, Drzezga A, Klockgether T, et al. Elevated *in vivo* [18F]-AV-1451 uptake in a patient with progressive supranuclear palsy. Mov Disord 2017; 32: 170–1.

Hansson O, Grothe MJ, Strandberg TO, Ohlsson T, Hägerström D, Jögi J, et al. Tau pathology distribution in Alzheimer's disease corresponds differentially to cognition-relevant functional brain networks. Front Neurosci 2017; 11: 167.

Hoenig MC, Bischof GN, Hammes J, Faber J, Fliessbach K, van Eimeren T, et al. Tau pathology and cognitive reserve in Alzheimer's disease. Neurobiol Aging 2017; 57: 1–7.

Illán I, Górriz J, Ramírez J, Salas-Gonzalez D, López M, Segovia F, et al. 18 F-FDG PET imaging analysis for computer aided Alzheimer's diagnosis. Inf Sci 2011; 181: 903–16.

Jones DT, Knopman DS, Gunter JL, Graff-Radford J, Vemuri P, Boeve BF, et al. Cascading network failure across the Alzheimer's disease spectrum. Brain 2016; 139: 547–62.

Lehmann M, Ghosh PM, Madison C, Laforce R, Corbetta-Rastelli C, Weiner MW, et al. Diverging patterns of amyloid deposition and hypometabolism in clinical variants of probable Alzheimer's disease. Brain 2013; 136: 844–58.

Leonardi N, Shirer WR, Greicius MD, Van De Ville D. Disentangling dynamic networks: separated and joint expressions of functional connectivity patterns in time. Hum Brain Mapp 2014; 35: 5984–95.

Lim HK, Nebes R, Snitz B, Cohen A, Mathis C, Price J, et al. Regional amyloid burden and intrinsic connectivity networks in cognitively normal elderly subjects. Brain 2014; 137: 3327–38.

Liu L, Drouet V, Wu JW, Witter MP, Small SA, Clelland C, et al. Trans-synaptic spread of tau pathology *in vivo*. PLoS One 2012; 7: e31302.

McKeown MJ, Hansen LK, Sejnowsk TJ. Independent component analysis of functional MRI: what is signal and what is noise? Curr Opin Neurobiol 2003; 13: 620–9.

McKhann GM, Knopman DS, Chertkow H, Hyman BT, Jack CR Jr, Kawas CH, et al. The diagnosis of dementia due to Alzheimer's disease: recommendations from the National Institute on Aging-Alzheimer's Association workgroups on diagnostic guidelines for Alzheimer's disease. Alzheimers Dement 2011; 7: 263–9.

Menkes-Caspi N, Yamin HG, Kellner V, Spires-Jones TL, Cohen D, Stern EA. Pathological tau disrupts ongoing network activity. Neuron 2015; 85: 959–66.

Ossenkoppele R, Schonhaut DR, Schöll M, Lockhart SN, Ayakta N, Baker SL, et al. Tau PET patterns mirror clinical and neuroanatomical variability in Alzheimer's disease. Brain 2016; 139 (Pt 5): 1551–67.

Pagani M, Öberg J, De Carli F, Calvo A, Moglia C, Canosa A, et al. Metabolic spatial connectivity in amyotrophic lateral sclerosis as revealed by independent component analysis. Hum Brain Mapp 2016; 37: 942–53.

Palop JJ, Chin J, Mucke L. A network dysfunction perspective on neurodegenerative diseases. Nature 2006; 443: 768–73.

Passamonti L, Rodrıguez PV, Hong YT, Allinson KS, Williamson D, Borchert RJ, et al. 18 F-AV-1451 positron emission tomography in Alzheimer's disease and progressive supranuclear palsy. Brain 2017; 140: 781–91.

Rohr CS, Okon-Singer H, Craddock RC, Villringer A, Margulies DS. Affect and the brain's functional organization: a resting-state connectivity approach. PLoS One 2013; 8: e68015.

Savio A, Fünger S, Tahmasian M, Rachakonda S, Manoliu A, Sorg C, et al. Resting state networks as simultaneously measured with fMRI and PET. J Nucl Med 2017; 58: 1314–17.

Schöll M, Lockhart SN, Schonhaut DR, O'Neil JP, Janabi M, Ossenkoppele R, et al. PET imaging of tau deposition in the aging human brain. Neuron 2016; 89: 971–82.

Seeley WW, Crawford RK, Zhou J, Miller BL, Greicius MD. Neurodegenerative diseases target large-scale human brain networks. Neuron 2009; 62: 42–52.

Shaffer JL, Petrella JR, Sheldon FC, Choudhury KR, Calhoun VD, Coleman RE, et al. Predicting cognitive decline in subjects at risk for Alzheimer disease by using combined cerebrospinal fluid, MR imaging, and PET biomarkers. Radiology 2013; 266: 583–91.

Shi F, Liu B, Zhou Y, Yu C, Jiang T. Hippocampal volume and asymmetry in mild cognitive impairment and Alzheimer's disease: meta-analyses of MRI studies. Hippocampus 2009; 19: 1055–64.

Shimada H, Kitamura S, Shinotoh H, Endo H, Niwa F, Hirano S, et al. Association between Aβ and tau accumulations and their influence on clinical features in aging and Alzheimer disease spectrum brains: a [11 C] PBB3-PET study. Alzheimers Dement 2017; 6: 11–20.

Shirer W, Ryali S, Rykhlevskaia E, Menon V, Greicius M. Decoding subject-driven cognitive states with whole-brain connectivity patterns. Cereb Cortex 2012; 22: 158–65.

Sperling RA, LaViolette PS, O'Keefe K, O'Brien J, Rentz DM, Pihlajamaki M, et al. Amyloid deposition is associated with impaired default network function in older persons without dementia. Neuron 2009; 63: 178–88.

Särelä J, Vigário R. Overlearning in marginal distribution-based ICA: analysis and solutions. J Mach Learn Res 2003; 4: 1447–69.

Teipel S, Grothe MJ, Initiative AsDN. Does posterior cingulate hypometabolism result from disconnection or local pathology across preclinical and clinical stages of Alzheimer's disease? Eur J Nucl Med Mol Imaging 2016; 43: 526–36.

Thal DR, Rüb U, Orantes M, Braak H. Phases of Aβ-deposition in the human brain and its relevance for the development of AD. Neurology 2002; 58: 1791–800.

Toussaint P-J, Perlbarg V, Bellec P, Desarnaud S, Lacomblez L, Doyon J, et al. Resting state FDG-PET functional connectivity as an early biomarker of Alzheimer's disease using conjoint univariate and independent component analyses. Neuroimage 2012; 63: 936–46.

Tzourio-Mazoyer N, Landeau B, Papathanassiou D, Crivello F, Etard O, Delcroix N, et al. Automated anatomical labeling of activations in SPM using a macroscopic anatomical parcellation of the MNI MRI single-subject brain. Neuroimage 2002; 15: 273–89.

Yakushev I, Chételat G, Fischer FU, Landeau B, Bastin C, Scheurich A, et al. Metabolic and structural connectivity within the default mode network relates to working memory performance in young healthy adults. Neuroimage 2013; 79: 184–90.

Yan C, Zang Y. DPARSF: a MATLAB toolbox for "pipeline" data analysis of resting-state fMRI. Front Syst Neurosci 2010; 4: 13.

Zhang H-Y, Wang S-J, Liu B, Ma Z-L, Yang M, Zhang Z-J, et al. Resting brain connectivity: changes during the progress of Alzheimer disease 1. Radiology 2010; 256: 598–606.

Zhou J, Greicius MD, Gennatas ED, Growdon ME, Jang JY, Rabinovici GD, et al. Divergent network connectivity changes in behavioural variant frontotemporal dementia and Alzheimer's disease. Brain 2010; 133: 1352–67.